Systematic design and experimental realization of multiplexed acoustic double-zero-index metamaterials

Yifan Tang,[1,2] Bin Liang,[2,*] Xuefeng Zhu,[3,†] and Shuyu Lin[1,‡]

[1]*Shaanxi Key Laboratory of Ultrasonics, Institute of Applied Acoustics, Shaanxi Normal University, Xi'an 710119, People's Republic of China*

[2]*Key Laboratory of Modern Acoustics, MOE, Institute of Acoustics, Department of Physics, Collaborative Innovation Center of Advanced Microstructures, Nanjing University, Nanjing 210093, People's Republic of China*

[3]*School of Physics and Innovation Institute, Huazhong University of Science and Technology, Wuhan, Hubei 430074, People's Republic of China*

An intriguing property of double-zero-index metamaterials (DZIMs) is that waves propagate through them without phase variation, which has received significant attention in wave-front and dispersion engineering. Recently, Dirac-like cone dispersion has been successfully exploited to realize a DZIM that operates only at a fixed frequency, while realizing DZIMs with multiple separated Dirac-like cones remains challenging. Here, we propose the first realization of a multiplexed acoustic double-zero-index metamaterial (MADM) capable of realizing three separated Dirac-like points at the Brillouin zone center for airborne sound. The resulting device is formed by introducing a series of blind holes with different heights, which are periodically arranged on the upper and lower parts of the waveguide. The underlying mechanism is that the proposed MADM possesses three Dirac-like cones derived from an accidental degeneracy of monopolar and dipolar resonances, which can be mapped to a DZIM with zero effective compressibility and mass density. We present an experimental realization of the designed MADM with three separated Dirac-like points, and demonstrate the functionality of the resulting device by means of extraordinary wave tunneling and acoustic focusing. We anticipate that our mechanism will offer the potential for designing multiplexed acoustic double-zero-index devices and may have substantial and profound applications in a variety of fields, such as ultrasonic therapy and acoustic communication.

I. INTRODUCTION

Metamaterials, with unprecedented effective parameters in electromagnetic, elastic, and acoustic wave systems, have been studied extensively in recent years to yield novel functionalities that are not easily achievable with natural materials [1–20]. Material parameters such as bulk modulus and mass density play an essential role in the behavior of acoustic waves as they propagate in a medium. Previous studies have shown that materials with single-negative dynamic mass density or the reciprocal of bulk modulus, which are called single-negative metamaterials, can be achieved with membrane-type metamaterials [21] and Helmholtz resonators [22]. A double-negative medium characterized by negative dynamic mass density and reciprocal of bulk modulus has been demonstrated utilizing coiling-up structures [23] and waveguides decorated with side holes and membranes [24].

The zero-index metamaterial has been of particular interest in the exploration of zero effective compressibility and mass density due to its great potential for realizing wave tunneling [25–28], cloaking of objects [29,30], and acoustic doping [31,32]. The single-zero-index metamaterial featuring only one dynamic parameter approaching zero can be realized by membrane-type structures [33] and anisotropic phononic crystals [34]; however, these are unsuitable for real applications because of the impedance mismatch. Double-zero-index metamaterials (DZIMs) possess higher transmission than single-zero-index metamaterials due to their finite effective impedance [35], which can be realized by doping the single-zero-index medium [36], coupling two Helmholtz resonators [37], and using parity-time symmetry [38]. Recently, the Dirac-like cone derived from an accidental degeneracy has been successfully leveraged to achieve DZIMs in wave systems [20,39–45]. The Dirac-like cone obtained from phononic crystals appears on two linearly dispersing bands accompanied by a dispersionless flat band, which is due to the accidental degeneracy of dipolar and monopolar resonances [46]. There is an intimate connection between

*liangbin@nju.edu.cn
†xfzhu@hust.edu.cn
‡sylin@snnu.edu.cn

the Dirac-like linear dispersion and double-zero index when the effective compressibility and mass density of a double-zero-index metamaterial are equal to zero [47]. However, most of the reported DZIMs have only one Dirac-like cone obtained from the presented individual unit, leading to a fixed operating frequency. Although efforts have been made to achieve DZIMs with two Dirac-like cones in elastic [48] and electromagnetic [49] systems, almost no research has been performed on DZIMs with three separated Dirac-like cones for airborne sound. Considering the diversity of practical problems such as ultrasonic therapy or acoustic communication that could call for a multiplexed acoustic double-zero-index metamaterial (MADM) to operate at different frequencies without reconfiguring the device shape, the realization of a highly efficient MADM is a fundamental and interesting area of research.

In this paper, we propose a MADM capable of realizing unusual wave transport properties at the frequencies of the three separated Dirac-like points. The resulting device is composed of a series of air blind holes of different heights arranged in a square lattice on the upper and lower parts of the air waveguide. The three separated Dirac-like cones with conical dispersion are demonstrated at the Γ point, which is derived from the degeneracy of dipolar and monopolar resonances. By employing the effective medium theory, the dynamic compressibility and mass density of the three Dirac-like points are verified to be close to zero at the same time. We demonstrate wave tunneling without phase variation inside the proposed DZIM and the convergence of acoustic energy without using gradient index metamaterials at three separated Dirac-like point frequencies, which directly reflect the DZIM's double-zero-index property. In the experimental verifications, a basic agreement between the measured acoustic intensity and pressure field distributions and the simulated results proves that the phase inside the resulting device remains constant.

II. DESIGN OF THE MADM AND MODEL ANALYSIS

Figure 1(a) schematically shows our designed MADM, which is composed of a series of air blind holes of different heights arranged in a square lattice on the upper and lower parts of the air waveguide. The meta unit with lattice constant a is outlined by the blue dotted box, and the yellow region represents the background medium, air. Figure 1(b) shows the individual unit cell containing a three-layer structure, where the top and bottom layers are composed of five blind holes and the middle layer is a cuboid air domain. In the current study, the height of the central blind hole is set at 16.65 mm for the top layer and 45.7 mm for the bottom layer, while the heights of surrounding blind holes are chosen as $h_1 = 16.8$ mm for the top layer and

$h_3 = 44.6$ mm for the bottom layer, respectively. The single blind hole radius R and the cuboid air domain thickness h_2 are chosen to be 13.5 mm and 23.85 mm, and the distance between the centers of the central blind hole and surrounding blind holes is set at $w = 29$ mm. Throughout this article, we employ the commercial software COMSOL Multiphysics for calculating the band structure of the meta unit and in the following simulations. The periodic boundary conditions are used on the meta-unit boundaries in the x-y plane to compute the band structure and eigenfields. With these geometrical parameters, the band structure of this unit cell is characterized by the existence of three separated Dirac-like points at three different frequencies, represented by the black points in Fig. 1(c). The square lattice system is fourfold rotationally symmetric, and the irreducible Brillouin zone of our proposed MADM is marked by triangle ΓXM. There are three accidental degeneracies marked by the green dashed boxes at frequencies of $f_1 = 0.4284c/a, f_2 = 0.8568c/a$, and $f_3 = 1.9876c/a$, where c is the sound speed of air. The Dirac-like point I demonstrates accidental degeneracy at the Brillouin zone center for the third, fourth, and fifth branches; Dirac-like point II shows accidental degeneracy at the Brillouin zone center for the eighth, ninth, and tenth branches; and the Dirac-like point III displays the accidental degeneracy for the twenty-fifth, twenty-sixth, and twenty-seventh branches at the Brillouin zone center. Figures 1(d)–1(f) show the dispersion surfaces in three dimensions to visualize Dirac-like cones I, II, and III in the k_x - k_y plane. The dispersion surfaces above and below the Dirac-like cones I, II, and III have positive and negative group velocities that intersect with flat bands marked in magenta at the same frequencies. Dirac-like points derived from the accidental degeneracy are theoretically analyzed by employing the multiple scattering theory. The Dirac-like cone at the Brillouin zone center requires linear dispersion accompanied by a flat band, which originates from the accidental degeneracy of the dipolar and monopolar modes. For the system under discussion, the angular momentum number m is equal to 0 and ± 1, corresponding to the monopolar and dipolar terms, respectively. The multiple scattering theory equations must satisfy the following matrix form [47]:

$$\begin{pmatrix} S_0 - 1/D_{-1} & -S_1 & S_2 \\ -S_{-1} & S_0 - 1/D_0 & -S_1 \\ S_{-2} & -S_{-1} & S_0 - 1/D_1 \end{pmatrix} \cdot \begin{pmatrix} b_{-1} \\ b_0 \\ b_1 \end{pmatrix} = 0. \tag{1}$$

Here, D_m is the T matrix, S_m represents the lattice sum with $S_{-m} = -S_m^*$, and b_m is the Mie scattering coefficient. The term D_1 equals D_{-1} because of the cylindrical symmetry of air blind holes, and the terms $S_{\pm 1}$ and $S_{\pm 2}$ equal to zero simultaneously at $\mathbf{k} = 0$ because of the lattice symmetry of the square lattice, where $\mathbf{k}$ is the wave vector. By solving Eq. (1), the monopolar mode and dipolar
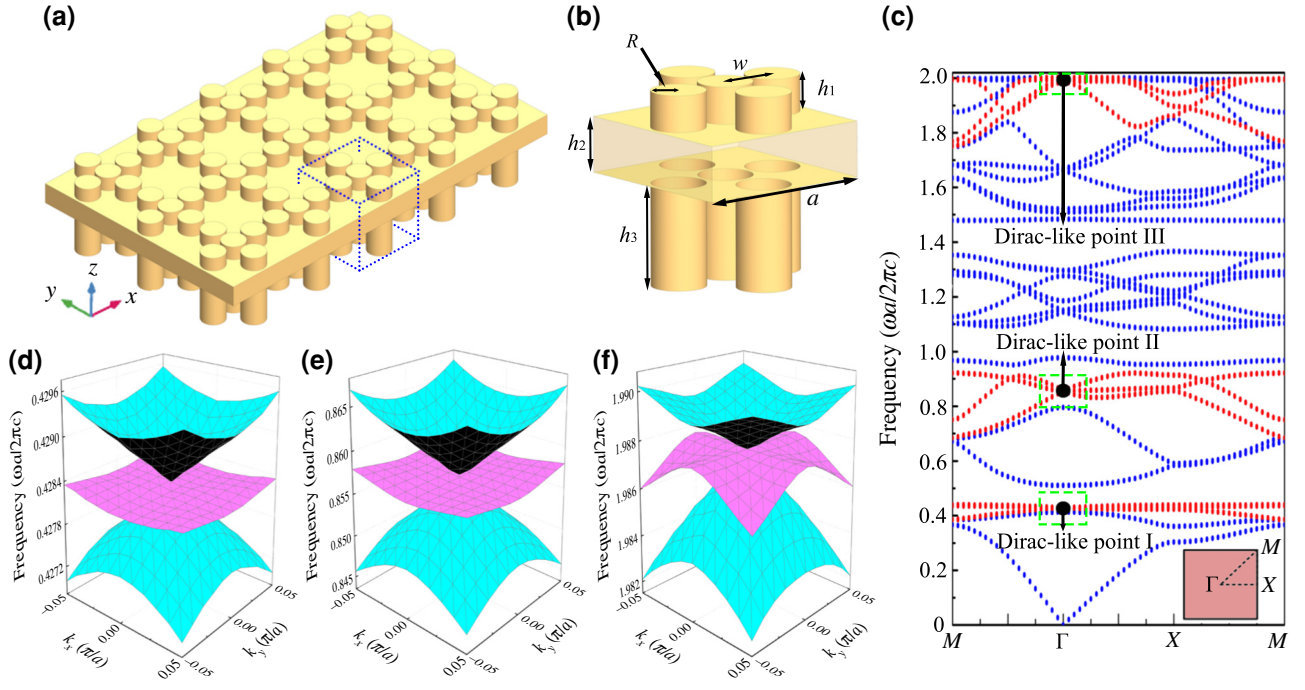
FIG. 1. (a) Schematic of our proposed MADM composed of periodically repeating primitive unit cells. The individual unit cell is shown by the blue dotted box, and the yellow region represents the background medium air. (b) An isometric view of an individual meta unit of the MADM containing ten blind holes. (c) Calculated band structure of the MADM. Three Dirac-like points are formed at the Γ point marked with black dots at frequencies $f_1 = 0.4284c/a$, $f_2 = 0.8558c/a$, and $f_3 = 1.9876c/a$. Inset: The first Brillouin zone of the square lattice. The enlarged view of 3D dispersion surfaces in the k_x-k_y plane near (d) the Dirac-like point I, (e) the Dirac-like point II, and (f) the Dirac-like point III.

modes at frequencie w_m and w_d where $S_0 - 1/D_0$ and $S_0 - 1/D_{\pm 1}$ are equal to zero. Perturbation methods can be employed to analyze the dispersion near $\mathbf{k} = 0$. Generally, the term D_0 does not equal $D_{\pm 1}$. The dispersion usually has three branches with quadratic dispersion, one of which is a monopolar mode and the other two are dipolar modes. When $S_0 = 1/D_0 = 1/D_{\pm 1}$ or $w_m = w_d = w^*$, accidental degeneracy occurs, leading to the change of the dispersion near $\mathbf{k} = 0$. We find that the dispersion $w_1 - w^* = 0 + O(\delta k^2)$ correlates with a flat band near the Γ point, and the two dispersions $w_{2,3} - w^* = \pm v_g \delta k + O(\delta k^2)$ have two bands of linear dispersions where the group velocities $\pm v_g$ are opposite and nonzero. Thus, the theory that accidental degeneracy leads to two linear dispersions accompanied by a flat band is established. It should be noted that we design the meta unit capable of realizing three separated Dirac-like points at the Γ point, where the Dirac-like point II frequency is exactly twice that of the Dirac-like point I. By appropriately modulating the geometrical parameters of the meta unit, the double-zero-index property of our proposed MADM can be configured to different frequencies accordingly.

To clarify the fundamental physics underlying the three-fold degenerate state, we compute the eigenfields of dipolar and monopolar modes near Dirac-like points I, II, and III, as demonstrated in Figs. 2(a)–2(i). It can be observed that each Dirac-like point consists of a threefold degeneracy with one monopolar mode and two orthogonal dipolar modes. It is worth noting that the symmetry of the square lattice, rather than the geometric parameters of the meta unit, affects the degeneracy of the dipolar modes. By changing the height of the air blind holes, the three separated Dirac-like cones at the Γ point created by accidental degeneracy of dipolar and monopolar states can be realized. For the monopolar mode of Dirac-like point I in Fig. 2(a), the central blind hole of the top layer has a relatively high pressure distribution at the frequency of $f_1 = 0.4284c/a$, which is caused by the local resonance. The bottom-layer blind holes show a relatively low pressure distribution, serving as off-resonance elements. For the two dipolar modes, Fig. 2(b) illustrates the longitudinal dipole whose pressure field is symmetrical along the x direction, while the pressure field of the transverse dipole is symmetrical along the y direction, as shown in Fig. 2(c). Next, we rotate the unit cell 180° along the x direction to get a better view. For the monopolar mode of the Dirac-like point II, the pressure field of the lower blind holes at $f_2 = 0.8568c/a$ manifests strong coupling in the cavities in Fig 2(d), while the ones with taller blind holes are negligibly influenced by the local resonance. Figures 2(e) and
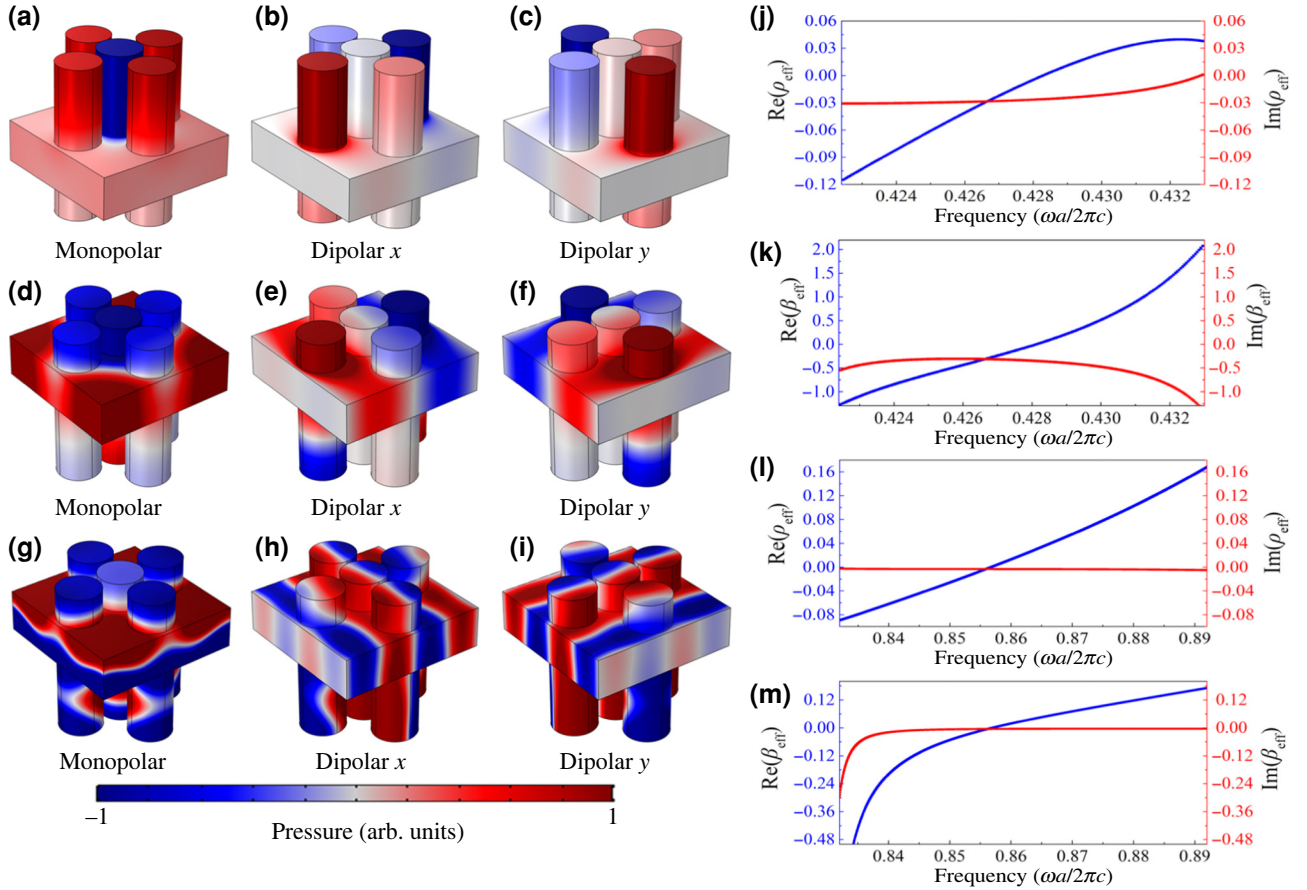
FIG. 2. The pressure field distributions of the monopolar mode and dipolar modes at (a)–(c) the Dirac-like point I, (d)–(f) the Dirac-like point II, and (g)–(i) the Dirac-like point III at frequencies of $f_1 = 0.4284c/a$, $f_2 = 0.8568c/a$, and $f_3 = 1.9876c/a$, respectively. The real and imaginary parts of the dynamic (j) mass density ρ_{eff} and (k) compressibility β_{eff} calculated in the vicinity of the frequency of the Dirac-like point I. The real and imaginary parts of the dynamic (l) mass density ρ_{eff} and (m) compressibility β_{eff} calculated near the Dirac-like point II frequency.

2(f) display the longitudinal dipole and transverse dipole whose pressure fields are symmetrical along the x direction and y direction, respectively. Figure 2(g) demonstrates the monopolar mode pressure field distribution of Dirac-like point III, which is the first-order waveguide mode. The first-order waveguide mode has an effective phase velocity of $v(\omega, h_2) = \left(\sqrt{1/c_0^2 - \pi^2/\omega^2 h_2^2} \right)^{-1}$, where h_2 is the thickness of the air waveguide, and c_0 and ω are the speed of sound in air and angular frequency, respectively. It can be recognized that the taller blind holes exhibit a faster phase velocity than the air waveguide around it. Figure 2(h) demonstrates the dipolar mode pressure field distribution is orthogonal to the one shown in Fig. 2(i) at the frequency $f_3 = 1.9876c/a$. The eigenmodes of the flat bands of the three Dirac-like points relevant to the transverse waves are illustrated in Figs. 2(c), 2(f), and 2(i), and these are deaf bands. We employ an effective parameter retrieval method to describe the physics of the resulting

device [50]. The monopolar state influences the reciprocal of the dynamic bulk modulus, while the dipolar state manipulates the dynamic mass density [51]. In previous studies, the thermal and viscous losses were very important [52–54]; therefore, we employ the narrow-region acoustics module to calculate the thermal and viscous losses of our proposed MADM. By introducing the narrow-region acoustics module, we calculate the real and imaginary parts of the effective compressibility and mass density near the frequencies of the Dirac-like points I and II. At the Dirac-like point I frequency $f_1 = 0.4284c/a$, it can be observed that both the dynamic compressibility β_{eff} and mass density ρ_{eff} are close to zero at the same time, as shown in Figs. 2(j) and 2(k). At the Dirac-like point II frequency $f_2 = 0.8568c/a$, the dynamic mass density ρ_{eff} and compressibility β_{eff} are indeed approaching zero simultaneously, as illustrated in Figs. 2(l) and 2(m). It is worth emphasizing that the imaginary parts of the effective compressibility and mass density near the frequency of the Dirac-like point I
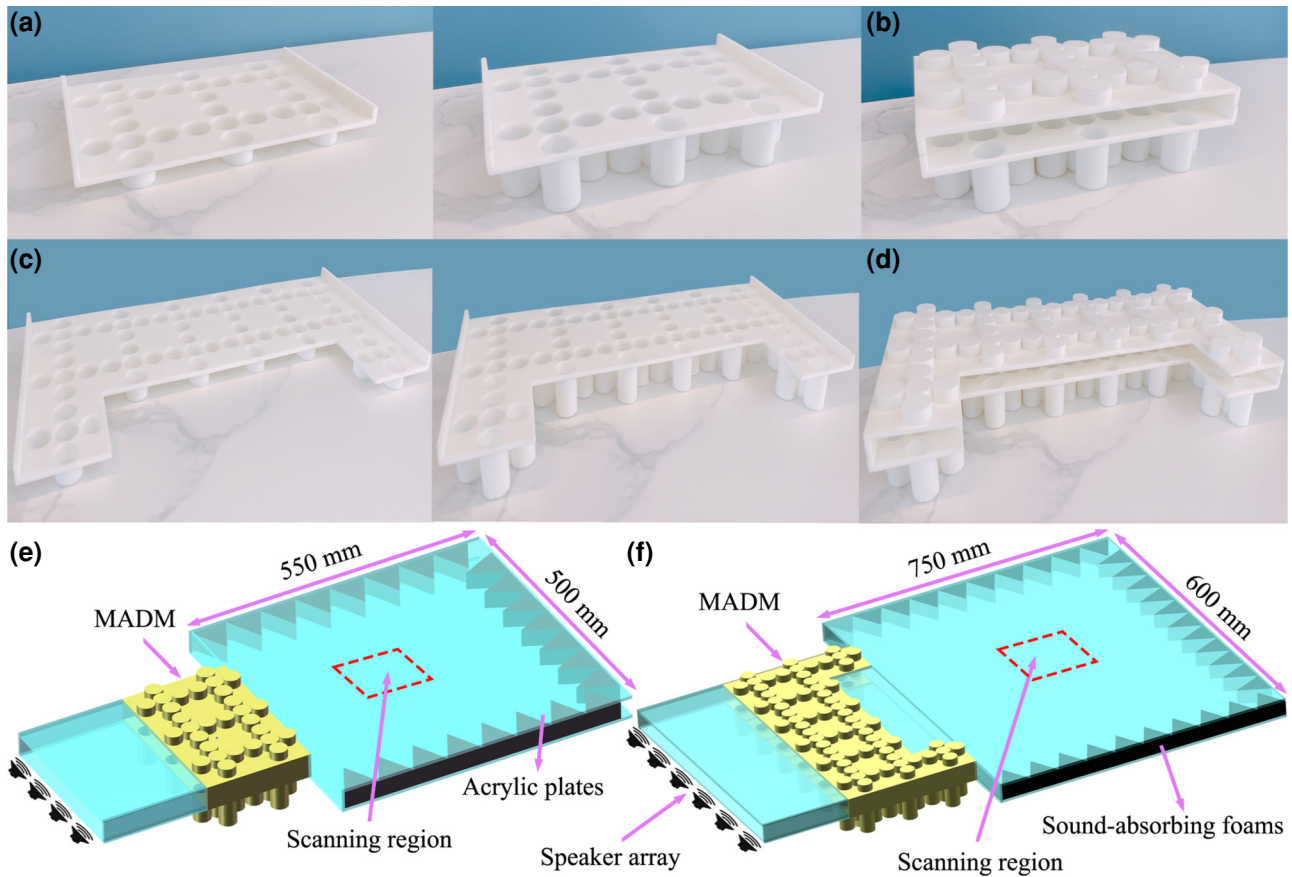
FIG. 3. (a) Photographs of the top and bottom 3D-printed samples of our proposed MADM with a size of $180 \times 280 \times 33.725$ mm^3 and $180 \times 280 \times 62.625$ mm^3, respectively. (b) Photograph of an experimental sample for achieving wave tunneling with a length of 180 mm in the x direction, a width of 280 mm in the y direction, and a height of 96.35 mm in the z direction. (c) Photos of the top and bottom layers of the proposed MADM with a size of $270 \times 550 \times 33.725$ mm^3 and $270 \times 550 \times 62.625$ mm^3. (d) Photograph of 3D-printed sample for achieving acoustic focusing with dimensions of 270, 550, and 96.35 mm in the x, y, and z directions, respectively. (e),(f) Schematic diagrams of the 3D experimental systems to realize wave tunneling and acoustic focusing. The experimental samples are placed in the middle of two rectangular waveguides.

are larger than those near the frequency of the Dirac-like point II.

III. EXPERIMENTAL SETUP

For the purpose of verifying the validity of our designed MADM, we carry out experiments to check the double-zero-index property at the frequencies of three separated Dirac-like points. Figure 3(a) depicts the schematic of the top and bottom layers of the MADM for achieving wave tunneling. The structure is made of acrylonitrile-butadiene-styrene plastic using the three-dimensional (3D) printing technique. The density of and speed of sound in acrylonitrile-butadiene-styrene plastic are 1230 kg/m^3 and 2230 m/s, and the acoustic impedance of the acrylonitrile-butadiene-styrene plastic is significantly larger than that of air. The wall thickness of the cylindrical blind holes and rectangular waveguide is 5 mm. The characteristic acoustic impedance of the acrylonitrile-butadiene-styrene

plastic is approximately 4 orders of magnitude larger than that of air, and the huge impedance mismatch between the acrylonitrile-butadiene-styrene plastic and air makes it possible for us to regard it as rigid. Figure 3(b) illustrates the experimental sample to demonstrate unusual wave tunneling functionality. The device consists of 2×3 unit cells with a size of $180 \times 280 \times 96.35$ mm^3. The top and bottom layers of the proposed MADM for achieving acoustic focusing are illustrated in Fig. 3(c); the MADM is built from 14 units by periodically repeating the meta unit to form a concave interface at the output side. The experimental sample of the proposed MADM to demonstrate the acoustic focusing effect with the size of $270 \times 550 \times 96.35$ mm^3 is shown in Fig. 3(d). Figures 3(e) and 3(f) are schematic illustrations of the 3D experimental systems for achieving wave tunneling and acoustic focusing, where the pressure field is measured in the scanning regions. Two arrays of loudspeakers are located 180 mm away from the experimental samples to generate
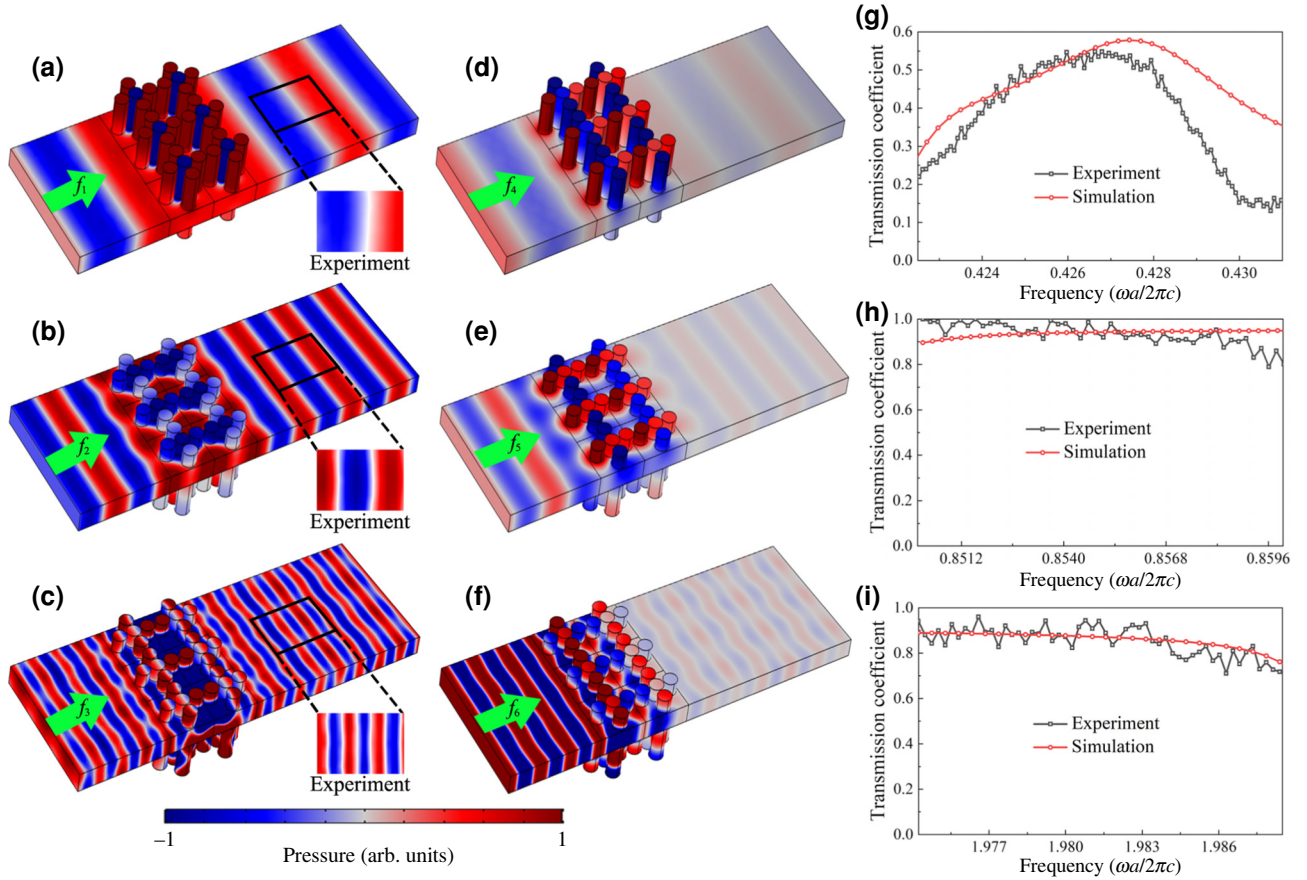
FIG. 4. The normalized pressure field distributions in the waveguide for the proposed MADM at frequencies of (a) $f_1 = 0.4284c/a$, (b) $f_2 = 0.8568c/a$, and (c) $f_3 = 1.9876c/a$. Insets: The corresponding experimentally measured results in the scanning regions labeled by black rectangles. The numerically simulated field distributions at the frequencies of (c) $f_4 = 0.4169c/a$, (d) $f_5 = 0.8192c/a$, and $f_6 = 1.5077c/a$, respectively. The direction of the incident waves is shown by the green arrows. The simulated and experimental transmission coefficients near the frequencies of (g) the Dirac-like point I, (h) the Dirac-like point II, and (i) the Dirac-like point III.

plane waves. The proposed MADMs for realizing wave tunneling and acoustic focusing are placed in the middle of two rectangular waveguides, which are composed of acrylic plates. A series of small holes in the x-y plane are drilled into the top acrylic plates to form the measurement area, which is a 130×90 mm^2 rectangular region. Two Bruel & Kjær type-4961 microphones with a 1/4-in. diameter are inserted into the rectangular waveguide through the holes to detect the sound field. One is installed on a 3D stepping motor that scans the measurement area point by point, while the other is placed near the loudspeakers as the reference signal. The phase and amplitude of the sound can be acquired from the cross spectrum of experimentally measured signals via the commercial software PULSE Labshop. Wedge-shaped pieces of foam are placed at three edges to absorb sound and mimic an anechoic environment.

IV. WAVE TUNNELING

As mentioned previously, the phase velocity is infinite in our designed MADM at the frequencies of three

separated Dirac-like points, which has significant practical applications in wave tunneling. In the vicinity of the three separated Dirac-like points, the Bloch wave vector has a relatively small magnitude, suggesting that the phase value in our proposed MADM remains almost constant, although it passes over a long distance. The normalized pressure field distributions of the MADM slab at the Dirac-like point I frequency ($f_1 = 0.4284c/a$), Dirac-like point II frequency ($f_2 = 0.8568c/a$), and Dirac-like point III frequency ($f_3 = 1.9876c/a$) are illustrated in Figs. 4(a)–4(c). Longitudinal plane waves of three different frequencies are generated from the input side at normal incidence, and plane-wave radiation boundary conditions are applied to the input and output sides of the waveguide. It is observed that the plane wave originating from the input side appears on the output side with no phase change after going through the MADM slab. The phase value of the wave is not accumulated in our proposed MADM slab since the phase velocity is almost infinite. As a consequence, there is no phase change in our proposed design, which is a clear indication of its double-zero-index characteristic. The
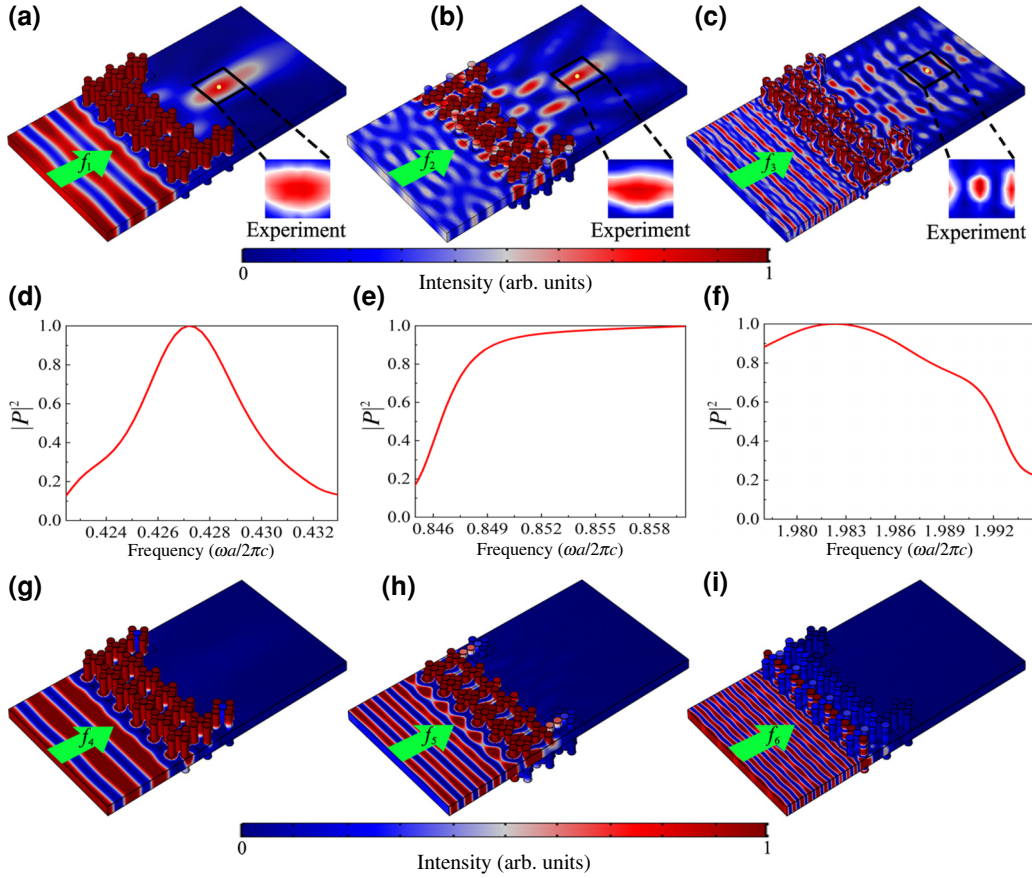
FIG. 5. The normalized intensity field distributions in the waveguide for the proposed MADM at frequencies of (a) $f_1 = 0.4284c/a$, (b) $f_2 = 0.8568c/a$, and (c) $f_3 = 1.9876c/a$. Insets: The corresponding experimentally measured results in the scanning regions labeled by black rectangles. The normalized sound intensity transmission property of the resulting device near the frequencies of (d) the Dirac-like point I, (e) the Dirac-like point II, and (f) the Dirac-like point III. The numerically simulated spatial distributions of the normalized intensity field at the frequencies of (g) $f_4 = 0.4169c/a$, (h) $f_5 = 0.8192c/a$, and (i) $f_6 = 1.5077c/a$. The direction of the incident waves is shown by the green arrows.

insets show the experimentally measured pressure field distributions, which are basically in accord with the numerically simulated results. The thermal and viscous losses and inevitable manufacturing and assembly faults are the major causes of experimental errors. It is confirmed that the plane wave front keeps its initial pattern as anticipated after traversing our proposed MADM at the frequencies of three separated Dirac-like cones. The phenomenon of wave tunneling realized by the resulting device reflects our proposed zero-index medium with the dynamic compressibility β_{eff} and mass density ρ_{eff} approaching zero simultaneously. In contrast, when the operating frequencies are modulated with a subtle deviation, i.e., $f_4 = 0.4169c/a$, $f_5 = 0.8192c/a$, and $f_6 = 1.5077c/a$, the comparative simulations show a noticeable increase of reflection, as illustrated in Figs 4(d)–4(f). The pressure field is mainly focused on the top-layer blind holes, as illustrated in Fig. 4(d), while the bottom-layer blind holes of our resulting device are not excited into resonant states. Figure 4(e) demonstrates that the pressure field is mainly

concentrated in the top-layer blind holes, while the bottom-layer blind holes manifest a near-zero pressure field. The majority of incident waves return to the input side after being reflected, as illustrated in Fig. 4(f), which results from the constructive interference of backscattered waves. It is worth emphasizing that the transmission effect of the DZIMs can be significantly modulated by changing the incident frequency. Figures 4(g)–4(i) demonstrate the transmission coefficients near the frequencies of the Dirac-like points I, II, and III under the narrow-region acoustics module, which are basically consistent with the experimental results. The transmission coefficients near the frequency of Dirac-like point I are smaller than those near the frequencies of Dirac-like points II and III.

V. ACOUSTIC FOCUSING

Finally, we examine the possibility of using our proposed MADM to mimic a concave lens by shaping the interface between the acoustic DZIM and air to control the

wave front of the transmitted wave. The transmitted wave is forced to propagate along its surface normal because of the concave interface at the metamaterial-air interface, which results in a focal point behind the MADM slab. Figures 5(a)–5(c) demonstrate the spatial distributions of the normalized intensity fields of our proposed MADM at the Dirac-like point I frequency ($f_1 = 0.4284c/a$), Dirac-like point II frequency ($f_2 = 0.8568c/a$), and Dirac-like point III frequency ($f_3 = 1.9876c/a$), where the focal points marked by the yellow dots are located 115, 210, and 255 mm away from our proposed MADM. The corresponding measured intensity field distributions at the frequencies of the three separated Dirac-like points are given in the insets. Owing to the size limitation of our translation platform, we measure the intensity fields in the regions marked by the black boxes. The reasonable agreement between the experimental data and the simulated results provides evidence that a remarkable acoustic focusing effect can be achieved with our designed MADM. To quantify the effectiveness of our concave lens, we calculate the intensity of the aforementioned three focus points corresponding to the frequencies of $f_1 = 0.4284c/a$, $f_2 = 0.8568c/a$, and $f_3 = 1.9876c/a$. The pressure intensity at the focus point of the wave is approximately 1.52 times stronger than that of the incident waves at the frequency of the Dirac-like point I, which directly reflects its acoustic focusing property. The pressure intensity at the focus point is around 2.87 times larger than that of the incident waves at the frequency of the Dirac-like point II, while at the frequency of the Dirac-like point III, the pressure intensity at the focus point is about 2.63 times the size of the incident waves. Figures 5(d)–5(f) demonstrate the normalized sound intensity transmission property as a function of frequency in the vicinity of the frequencies of the Dirac-like points I, II, and III, respectively. It can be observed that our proposed MADM can realize the convergence of acoustic energy at three separated Dirac-like points. When the frequencies of the incident waves deviate slightly from the frequencies of three separated Dirac-like points, it can be clearly observed that there is a significant accumulation of phase during propagation in the MADM. The spatial distributions of the normalized intensity fields at the frequencies of $f_4 = 0.4169c/a$, $f_5 = 0.8192c/a$, and $f_6 = 1.5077c/a$ are demonstrated in Figs. 5(g)–5(i). The incident waves are almost reflected into the entrance channel, and the air blind holes with different heights are not excited into resonant states, leading to an increase in reflection. Notably, unlike in the previous studies where acoustic focusing was realized by gradient index metamaterials, we accomplish acoustic energy convergence by shaping the interface of the MADM.

VI. CONCLUSIONS

In conclusion, we theoretically design and experimentally demonstrate a MADM with three separated Dirac-like cones at the Γ point for airborne sound, which is able to realize a double-zero-index property at three different frequencies without reconfiguring the device shape. Our proposed MADM consists of a series of air blind holes with different heights periodically arranged on the upper and lower parts of the air waveguide. Our proposed MADM exhibits three separated Dirac-like cones owing to the accidental degeneracy of two linear dispersion bands accompanied by a dispersionless flat band. We investigate some possible applications that are closely linked to the double-zero-index features of our designed DZIM. The effectiveness of the proposed DZIM is shown by generating remarkable effects at different frequencies, such as wave tunneling and acoustic focusing. By experimentally measuring the acoustic intensity and pressure fields in the scanning region, we demonstrate the reasonable agreement between the experimental data and the simulated results, which provides evidence of the realization of no phase accumulation in the proposed DZIM at three different frequencies. Our approach offers the potential for designing and applying MADM devices, which would possess a significant and far-reaching influence on a variety of practical application fields, such as medical ultrasonic therapy and acoustic communication.

[1] N. F. Yu, P. Genevet, M. A. Kats, F. Aieta, J. P. Tetienne, F. Capasso, and Z. Gaburro, Light propagation with phase discontinuities: Generalized laws of reflection and refraction, Science **334**, 333 (2011).

[2] H. Suchowski, K. O'Brien, Z. J. Wong, A. Salandrino, X. B. Yin, and X. Zhang, Phase mismatch–free nonlinear propagation in optical zero-index materials, Science **342**, 1223 (2013).

[3] G. C. Ma, M. Yang, S. W. Xiao, Z. Y. Yang, and P. Sheng, Acoustic metasurface with hybrid resonances, Nat. Mater. **13**, 873 (2014).

[4] B. Liang, X. S. Guo, J. Tu, D. Zhang, and J. C. Cheng, An acoustic rectifier, Nat. Mater. **9**, 989 (2010).

[5] Y. Li, K. J. Zhu, Y. G. Peng, W. Li, T. Z. Yang, H. X. Xu, H. Chen, X. F. Zhu, S. Z. Fan, and C. W. Qiu, Thermal meta-device in analogue of zero-index photonics, Nat. Mater. **18**, 48 (2019).

[6] S. A. Cummer, J. Christensen, and A. Alù, Controlling sound with acoustic metamaterials, Nat. Rev. Mater. **1,** 16001 (2016).

[7] B. Assouar, B. Liang, Y. Wu, Y. Li, J. C. Cheng, and Y. Jing, Acoustic metasurfaces, Nat. Rev. Mater. **3,** 460 (2018).

[8] B. Liang, B. Yuan, and J. C. Cheng, Acoustic diode: Rectification of acoustic energy flux in one-dimensional systems, Phys. Rev. Lett. **103,** 104301 (2009).

[9] X. F. Zhu, B. Liang, W. F. Kan, X. Y. Zou, and J. C. Cheng, Acoustic cloaking by a superlens with single-negative materials, Phys. Rev. Lett. **106,** 014301 (2011).

[10] X. F. Zhu, K. Li, P. Zhang, J. Zhu, J. T. Zhang, C. Tian, and S. C. Liu, Implementation of dispersion-free slow acoustic wave propagation and phase engineering with helical-structured metamaterials, Nat. Commun. **7,** 11731 (2016).

[11] Y. Li, B. Liang, Z. M. Gu, X. Y. Zou, and J. C. Cheng, Reflected wavefront manipulation based on ultrathin planar acoustic metasurfaces, Sci. Rep. **3,** 2546 (2013).

[12] X. D. Fan, Y. F. Zhu, Z. H. Su, N. Li, X. L. Huang, Y. Kang, C. Li, C. S. Weng, H. Zhang, and B. Liang, Ultrabroadband and reconfigurable transmissive acoustic metascreen, Adv. Funct. Mater. **33,** 2300752 (2023).

[13] Y. F. Tang, Y. F. Zhu, B. Liang, J. Yang, J. Yang, and J. C. Cheng, One-way acoustic beam splitter, Sci. Rep. **8,** 13573 (2018).

[14] Y. F. Zhu, N. J. Gerard, X. X. Xia, G. C. Stevenson, L. Cao, S. W. Fan, C. M. Spadaccini, Y. Jing, and B. Assouar, Systematic design and experimental demonstration of transmission-type multiplexed acoustic metaholograms, Adv. Funct. Mater. **31,** 2101947 (2021).

[15] X. Jiang, Y. Li, B. Liang, J. C. Cheng, and L. K. Zhang, Convert acoustic resonances to orbital angular momentum, Phys. Rev. Lett. **117,** 034301 (2016).

[16] Y. F. Tang, Y. Tian, and S. Y. Lin, Voltage-controlled density-near-zero piezoelectric metamaterials for wavefront shaping, acoustic splitting, focusing and doping, Appl. Phys. Express **15,** 074003 (2022).

[17] Z. H. Tian, C. Shen, J. F. Li, E. Reit, Y. Y. Gu, H. Fu, S. A. Cummer, and T. J. Huang, Programmable acoustic metasurfaces, Adv. Funct. Mater. **29,** 1808489 (2019).

[18] Y. F. Tang, B. Liang, and S. Y. Lin, Broadband ventilated meta-barrier based on the synergy of mode superposition and consecutive Fano resonances, J. Acoust. Soc. Am. **152,** 2412 (2022).

[19] Y. F. Zhu, J. Hu, X. D. Fan, J. Yang, B. Liang, X. F. Zhu, and J. C. Cheng, Fine manipulation of sound via lossy metamaterials with independent and arbitrary reflection amplitude and phase, Nat. Commun. **9,** 1632 (2018).

[20] C. Xu, H. Chu, J. Luo, Z. H. Hang, Y. Wu, and Y. Lai, Three-dimensional electromagnetic void space, Phys. Rev. Lett. **127,** 123902 (2021).

[21] Z. Y. Yang, J. Mei, M. Yang, N. H. Chan, and P. Sheng, Membrane-type acoustic metamaterial with negative dynamic mass, Phys. Rev. Lett. **101,** 204301 (2008).

[22] N. Fang, D. J. Xi, J. Y. Xu, M. Ambati, W. Srituravanich, C. Sun, and X. Zhang, Ultrasonic metamaterials with negative modulus, Nat. Mater. **5,** 452 (2006).

[23] Z. X. Liang and J. Li, Extreme acoustic metamaterial by coiling up space, Phys. Rev. Lett. **108,** 114301 (2012).

[24] S. H. Lee, C. M. Park, Y. M. Seo, Z. G. Wang, and C. K. Kim, Composite acoustic medium with simultaneously negative density and modulus, Phys. Rev. Lett. **104,** 054301 (2010).

[25] R. Fleury and A. Alù, Extraordinary sound transmission through density-near-zero ultranarrow channels, Phys. Rev. Lett. **111,** 055501 (2013).

[26] X. F. Zhu, Effective zero index in locally resonant acoustic material, Phys. Lett. A **377,** 1784 (2013).

[27] Y. Li, Y. Wu, and J. Mei, Double Dirac cones in phononic crystals, Appl. Phys. Lett. **105,** 014107 (2014).

[28] F. M. Liu, X. Q. Huang, and C. T. Chan, Dirac cones at k→= in acoustic crystals and zero refractive index acoustic materials, Appl. Phys. Lett. **100,** 071911 (2012).

[29] L. Y. Zheng, Y. Wu, X. Ni, Z. G. Chen, M. H. Lu, and Y. F. Chen, Acoustic cloaking by a near-zero-index phononic crystal, Appl. Phys. Lett. **104,** 161904 (2014).

[30] W. Zhao, Y. T. Yang, Z. Tao, and Z. H. Hang, Tunable transmission and deterministic interface states in double-zero-index acoustic metamaterials, Sci. Rep. **8,** 6311 (2018).

[31] Z. M. Gu, H. Gao, T. Liu, Y. Li, and J. Zhu, Dopant-modulated sound transmission with zero index acoustic metamaterials, J. Acoust. Soc. Am. **148,** 1636 (2020).

[32] Z. Y. Wang, F. Yang, L. B. Liu, M. Kang, and F. M. Liu, Total transmission and total reflection of acoustic wave by zero index metamaterials loaded with general solid defects, J. Appl. Phys. **114,** 194502 (2013).

[33] Y. Gu, Y. Cheng, J. S. Wang, and X. J. Liu, Controlling sound transmission with density-near-zero acoustic membrane network, J. Appl. Phys. **118,** 024505 (2015).

[34] C. Q. Xu, S. B. Huang, Z. W. Guo, H. T. Jiang, Y. Li, Y. Wu, and H. Chen, Acoustic beam splitting and cloaking based on a compressibility-near-zero medium, Phys. Rev. Appl. **17,** 054025 (2022).

[35] C. Q. Xu, G. C. Ma, Z. G. Chen, J. Luo, J. J. Shi, Y. Lai, and Y. Wu, Three-dimensional acoustic double-zero-index medium with a fourfold degenerate Dirac-like point, Phys. Rev. Lett. **124,** 074501 (2020).

[36] Y. D. Xu and H. Y. Chen, Total reflection and transmission by epsilon-near-zero metamaterials with defects, Appl. Phys. Lett. **98,** 113501 (2011).

[37] W. Q. Wang, X. S. Fang, N. Y. Wang, Y. Li, and T. Hao, Broadband acoustic double-zero-index cloaking with coupled Helmholtz resonators, New J. Phys. **24,** 083032 (2022).

[38] J. Luo, J. Li, and Y. Lai, Electromagnetic impurity-immunity induced by parity-time symmetry, Phys. Rev. X **8,** 031035 (2018).

[39] M. Dubois, C. Z. Shi, X. F. Zhu, Y. Wang, and X. Zhang, Observation of acoustic Dirac-like cone and double zero refractive index, Nat. Commun. **8,** 14871 (2017).

[40] C. Q. Xu and Y. Lai, Configurable Dirac-like conical dispersions in complex photonic crystals, Phys. Rev. B **95,** 045124 (2017).

[41] Y. Li and J. Mei, Double Dirac cones in two-dimensional dielectric photonic crystals, Opt. Express **23,** 12089 (2015).

[42] C. T. Chan, X. Q. Huang, F. M. Liu, and Z. H. Hang, Dirac dispersion and zero-index in two dimensional and

three dimensional photonic and phononic systems, Prog. Electromagn. Res. B **44**, 163 (2012).

[43] Y. Li, S. Kita, P. Muñoz, O. Reshef, D. I. Vulis, M. Yin, M. Lončar, and E. Mazur, On-chip zero-index metamaterials, Nat. Photonics **9**, 738 (2015).

[44] J. Mei, Y. Wu, C. T. Chan, and Z. Q. Zhang, First-principles study of Dirac and Dirac-like cones in phononic and photonic crystals, Phys. Rev. B **86**, 035141 (2012).

[45] H. Zhu and F. Semperlotti, Double-zero-index structural phononic waveguides, Phys. Rev. Appl. **8**, 064031 (2017).

[46] F. M. Liu, Y. Lai, X. Q. Huang, and C. T. Chan, Dirac cones at $k = 0$ in phononic crystals, Phys. Rev. B **84**, 224113 (2011).

[47] X. Q. Huang, Y. Lai, Z. H. Hang, H. H. Zheng, and C. T. Chan, Dirac cones induced by accidental degeneracy in photonic crystals and zero-refractive-index materials, Nat. Mater. **10**, 582 (2011).

[48] B. Li, Z. Li, J. Christensen, and K. T. Tan, Dual Dirac cones in elastic Lieb-like lattice metamaterials, Appl. Phys. Lett. **114**, 081906 (2019).

[49] J. A. Rodríguez, B. Wang, and M. A. Cappelli, Dual-polarization Dirac cones in a simple 2D square lattice photonic crystal, Opt. Lett. **45**, 2486 (2020).

[50] V. Fokin, M. Ambati, C. Sun, and X. Zhang, Method for retrieving effective properties of locally resonant acoustic metamaterials, Phys. Rev. B **76**, 144302 (2007).

[51] Y. Cheng, C. Zhou, B. G. Yuan, D. J. Wu, Q. Wei, and X. J. Liu, Ultra-sparse metasurface for high reflection of low-frequency sound based on artificial Mie resonances, Nat. Mater. **14**, 1013 (2015).

[52] M. Malléjac, A. Merkel, J. Sánchez-Dehesa, J. Christensen, V. Tournat, V. Romero-García, and J.-P. Groby, Experimental evidence of a hiding zone in a density-near-zero acoustic metamaterial, J. Appl. Phys. **129**, 145101 (2021).

[53] M. Mallejac, A. Merkel, J. Sanchez-Dehesa, J. Christensen, V. Tournat, J.-P. Groby, and V. Romero-García, Zero-phase propagation in realistic plate-type acoustic metamaterials, Appl. Phys. Lett. **115**, 134101 (2019).

[54] M. Malléjac, A. Merkel, V. Tournat, J.-P. Groby, and V. Romero-García, Doping of a plate-type acoustic metamaterial, Phys. Rev. B **102**, 060302 (2020).